Title

X-ray Fluorescence Computed Tomography (XFCT) Imaging with a Superfine Pencil Beam X-ray Source

Journal

Photonics, 8(7)

ISSN

2304-6732

Authors

Romero, Ignacio O
Fang, Yile
Lun, Michael
et al.

Publication Date

2021

DOI

10.3390/photonics8070236

Peer reviewed

photonics

MDPI

Article

X-ray Fluorescence Computed Tomography (XFCT) Imaging with a Superfine Pencil Beam X-ray Source

Ignacio O. Romero, Yile Fang, Michael Lun and Changqing Li *

Department of Bioengineering, University of California, Merced, CA 95343, USA; iromero7@ucmerced.edu (I.O.R.); yfang15@ucmerced.edu (Y.F.); mlun@ucmerced.edu (M.L.)
* Correspondence: cli32@ucmerced.edu

Abstract: X-ray fluorescence computed tomography (XFCT) is a molecular imaging technique that can be used to sense different elements or nanoparticle (NP) agents inside deep samples or tissues. However, XFCT has not been a popular molecular imaging tool because it has limited molecular sensitivity and spatial resolution. We present a benchtop XFCT imaging system in which a superfine pencil-beam X-ray source and a ring of X-ray spectrometers were simulated using GATE (Geant4 Application for Tomographic Emission) Monte Carlo software. An accelerated majorization minimization (MM) algorithm with an L^1 regularization scheme was used to reconstruct the XFCT image of molybdenum (Mo) NP targets. Good target localization was achieved with a DICE coefficient of 88.737%. The reconstructed signal of the targets was found to be proportional to the target concentrations if detector number, detector placement, and angular projection number are optimized. The MM algorithm performance was compared with the maximum likelihood expectation maximization (ML-EM) and filtered back projection (FBP) algorithms. Our results indicate that the MM algorithm is superior to the ML-EM and FBP algorithms. We found that the MM algorithm was able to reconstruct XFCT targets as small as 0.25 mm in diameter. We also found that measurements with three angular projections and a 20-detector ring are enough to reconstruct the XFCT images.

Keywords: X-ray fluorescence; computed tomography; GATE; Geant4; image reconstruction; X-ray imaging

Citation: Romero, I.O.; Fang, Y.; Lun, M.; Li, C. X-ray Fluorescence Computed Tomography (XFCT) Imaging with a Superfine Pencil Beam X-ray Source. *Photonics* **2021**, *8*, 236. https://doi.org/10.3390/photonics8070236

Received: 15 May 2021
Accepted: 22 June 2021
Published: 25 June 2021

1. Introduction

X-ray fluorescence computed tomography (XFCT) is a molecular imaging technique of X-ray photons that can be used to sense different elements or nanoparticle agents inside deep samples or tissues. XFCT has been an active research topic for many years. XFCT imaging quantifies and maps the distribution of a high-atomic-number (Z) element of interest in objects. Many XFCT benchtop systems employ a cone-beam source geometry, with pinhole detector collimation to reduce the imaging time and dose [1–3]. However, pencil-beam geometry provides greater spatial resolution due to the radiation of a line rather than a volume at the cost of a longer scan time. Upon X-ray excitation, element specific characteristic X-rays are emitted from a target and then recorded. Ideally, multiple spectral detectors are configured to optimize the detected X-ray fluorescent signal, reduce scatter detection, and reduce the scan time and dose delivered to the imaging object [4,5]. Compton scattering is a prevalent source of noise in XFCT imaging. Unlike the fluorescent signal, Compton scattering does not have a fixed energy and does not have isotropic emissions. Generally, as the incident beam energy is increased, the Compton scattering becomes more forward scattering [5]. The scattered signal can significantly hinder the fluorescent signal if the detector placement is not optimized in an orthogonal configuration or in a backscatter configuration [5].

Nanoparticles such as molybdenum (Mo) and gold (Au) nanoparticles (NPs) have attracted significant attention in biomedical imaging. The K-shell emission energies of these NPs have greater penetrability, which enables deeper functional tissue imaging. The

high biocompatibility of MoNPs and AuNPs allows for greater injection doses with fewer concerns of cell toxicity, which makes it feasible for the NPs to act as both CT contrast agents and functional imaging contrast agents [6,7]. For many cancer imaging applications, the NPs are used as passive targeting agents due to the enhanced permeability and retention (EPR) effects of the tumor [5]. AuNPs have been extensively investigated due to their high affinity ligands, which have led to dose enhancements in radiation cancer treatment [3,7–9].

A simple filtered back projection (FBP) reconstruction can be performed to obtain the X-ray fluorescent computed tomography (XFCT) image [10–12]. A popular iterative method to reconstruct the emission tomographic image is the maximum likelihood expectation maximization (ML-EM) algorithm [1–4,13]. Recently, a Nesterov accelerated MM algorithm with an L^1 regularization known as fNUMOS (fast NonUniform Multiplicative MM algorithm with Ordered Subsets acceleration) has shown success in X-ray luminescence computed tomography (XLCT) image reconstruction [14,15]. The MM algorithm with the Nesterov acceleration technique guarantees monotonicity and improves the convergence rate by limiting computational exhaustive matrix operations on the system matrix while promoting sparsity with the L^1 regularization [16,17].

In this work, a benchtop XFCT imaging system is presented in which a quasi-monochromatic pencil-beam X-ray source from Sigray, Inc. and a ring of spectrometers were simulated using the GATE (Geant4 Application for Tomographic Emission) Monte Carlo software [18]. A quasi-monochromatic X-ray source spectrum was simulated due to the emergence of compact quasi-monochromatic sources in laboratory settings, which enhance CT image quality [19]. The X-ray propagation inside the media was modeled to construct the system matrix. The XFCT image of two MoNP targets embedded in a cylindrical water phantom was reconstructed. The number of detectors used for the reconstruction was varied to show the detector number and position dependence on the reconstruction image quality. The images from the simulations were reconstructed using the fNUMOS algorithm and compared with the ML-EM and FBP algorithms. The target size was then reduced to show the capabilities of high spatial resolution imaging with the current setup. The angular projection number was also varied among 3, 6, and 10 projections, which are practically relevant projection numbers for pencil-beam XFCT imaging.

This paper is organized as follows. In Section 2, the methods of the GATE simulation using the unique Sigray source and ring detector configuration are presented. In Section 3, the results showing the effects of detector number and placement and the results comparing the fNUMOS reconstruction algorithm to ML-EM and FBP reconstructions are presented. Section 3 also shows the results of the high spatial resolution imaging in which the target size was reduced and the angular projection number was varied. The paper concludes with a discussion of the results and future works.

2. Materials and Methods

2.1. GATE Simulation

The GATE Monte Carlo software was developed by the international OpenGATE collaboration as a GEANT4 wrapper that encapsulates the GEANT4 libraries specific to medical imaging and radiotherapy researchers [18]. GATE utilizes the macro language to ease the learning curve of GEANT4 and allows GEANT4 toolkits to be more accessible to medical imaging and radiotherapy researchers [18]. GATE has now allowed for the design and optimization of new medical imaging devices and radiotherapy protocols [18].

The GATE simulations in this work were parallelized and executed with a custom bash script on a 20 CPU workstation. The simulation wait time was approximately two days. The physics lists enabled in GATE consisted of the photoelectric effect, Compton scattering, and Rayleigh scattering, which are the primary physics processes accounted for in XFCT imaging. To observe characteristic X-rays, atom de-excitation was enabled under the photoelectric effect process. The GATE software stores all output as ROOT files [20]. The necessary data from the ROOT output file was extracted using custom C++ code and processed in MATLAB. The extracted data consisted of the detector element number, the

deposited energy, and the angular projection number. The number of data sets needed were equal to the number of linear translations.

A schematic of the GATE simulation setup along with a GATE simulation snapshot is seen in Figure 1. For demonstration purposes, only 10 X-ray photons are shown in the GATE simulation snapshot. A 30 mm diameter cylindrical water phantom was positioned at the center of the reference frame. Two targets (T1, T2) with uniform 5 mg/mL and 10 mg/mL concentrations of MoNPs were embedded offset from the phantom center with the 5 mg/mL target (T1) closest to the phantom surface. The targets had a diameter and an edge-to-edge distance of 2 mm.

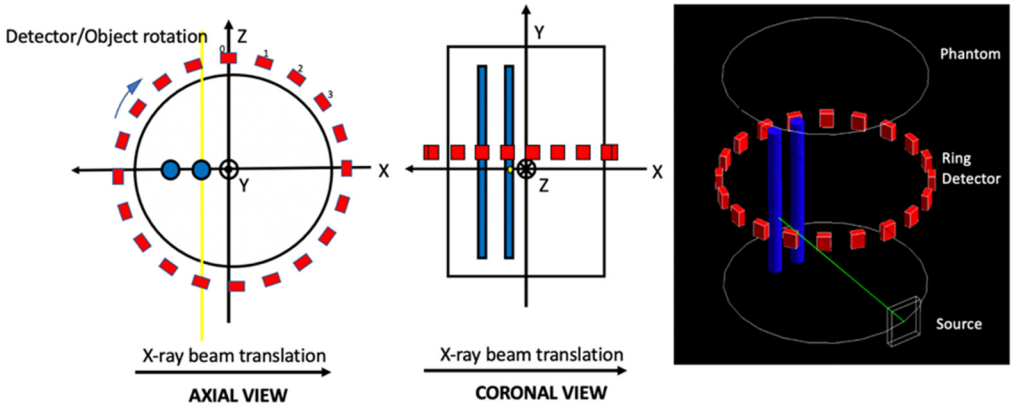

Figure 1. Axial view, coronal view, and snapshot (**right**) of the XFCT simulation setup in GATE. The axial view shows the X-ray beam as a yellow line and the coronal view shows the X-ray beam as a yellow dot near the center of the reference frame. The snapshot shows the trajectory of the X-ray photons as green lines.

The detector ring had a diameter of 31 mm and consisted of 20 cadmium zinc telluride (CZT) elements. A detailed schematic of the ring detector is seen in Figure 2. Each detector element had dimensions of $2 \times 2 \times 1$ mm^3. The X-ray beam size along the x-axis was 100 µm. The pencil beam had a divergence angle of 0.05°. A total of 10^7 X-ray photons per step were initialized. The X-ray beam scanned 2 mm below the detector ring. The linear step size was 125 µm; therefore, 248 linear steps were acquired to cover the phantom diameter and phantom edge. Six angular projections were acquired with a 30° angular step size. In this setup, the detector ring was allowed to rotate with the phantom about the center of the reference frame, whereas the X-ray beam translated linearly only.

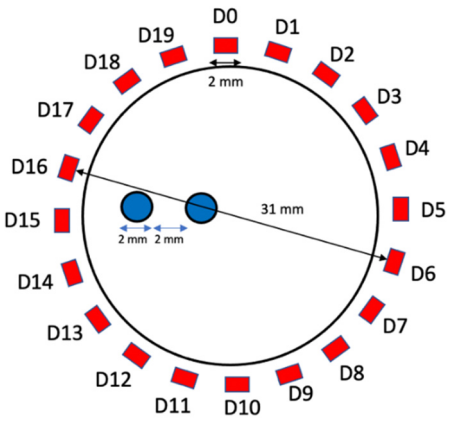

Figure 2. Schematic of the cadmium zinc telluride (CZT) ring detector.

The object was scanned by a modeled Sigray source from Sigray, Inc. The Sigray source was modeled using the linear interpolation user spectrum tool from GATE. The energy of the emitted photon is determined according to a probability distribution created by piecewise-linear interpolation between the energies provided. The modeled Sigray source spectrum is seen in Figure 3. The details of the source can be found at (https://sigray.com, accessed on 15 May 2021). In summary, the target anode and the company's optics allow for an X-ray flux of up to 10^9 photons per second. The target anode is composed of a silver microstructure encapsulated in a diamond substrate, which allows for a higher heat load limit and thus greater bombardment of electrons. The company optics consist of a monocapillary lens, which allows for a clean, low-energy cut off.

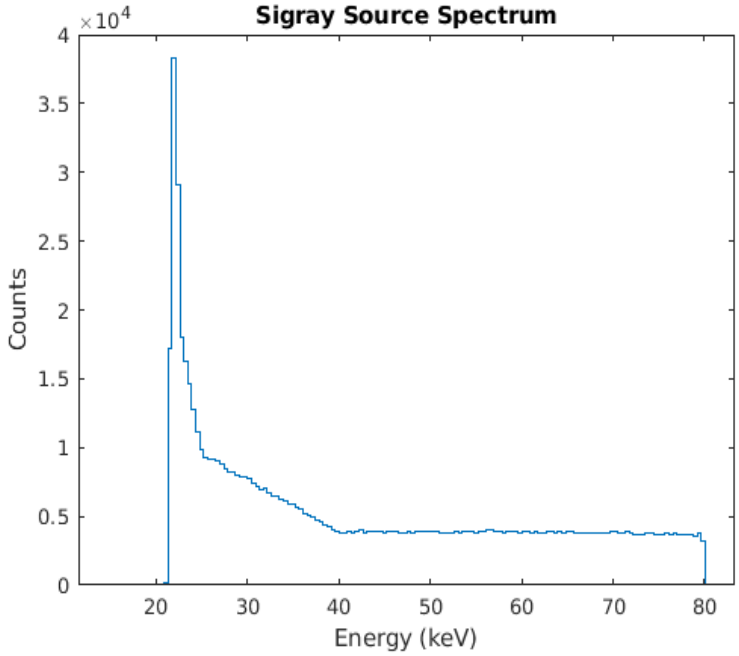

Figure 3. X-ray spectrum of a typical X-ray source from Sigray, Inc.

Before generating the X-ray fluorescent sinogram for reconstruction, the removal of scattered X-ray photons was applied on each measurement at each linear scan step by fitting X-ray photon energies in an 8 keV energy window. The 8 keV energy window was centered on the brightest fluorescent peak of the target element, which was 17.48 keV. A 4th-order polynomial was used to fit the scattered X-ray spectrum (the scattered X-ray source energy), which was subtracted from the measured energy spectrum to obtain the measured X-ray fluorescent photon energy spectrum. An example of the removal is seen in Figure 4a. The net counts curve was shifted downward to avoid overlap with the total count curve for better view. Due to the unique spectrum of the Sigray source, little to no scattering was observed in the 8 keV energy window. Figure 4b is a zoomed-in version of Figure 4a, which focuses on the energy range of the MoNP fluorescent energy. Only the counts bounded by the red dashed vertical lines were collected for the sinogram. The width between the red dashed vertical lines corresponds to the energy resolution of the detector elements, which was 200 eV. The sinogram is seen in Figure 4c.

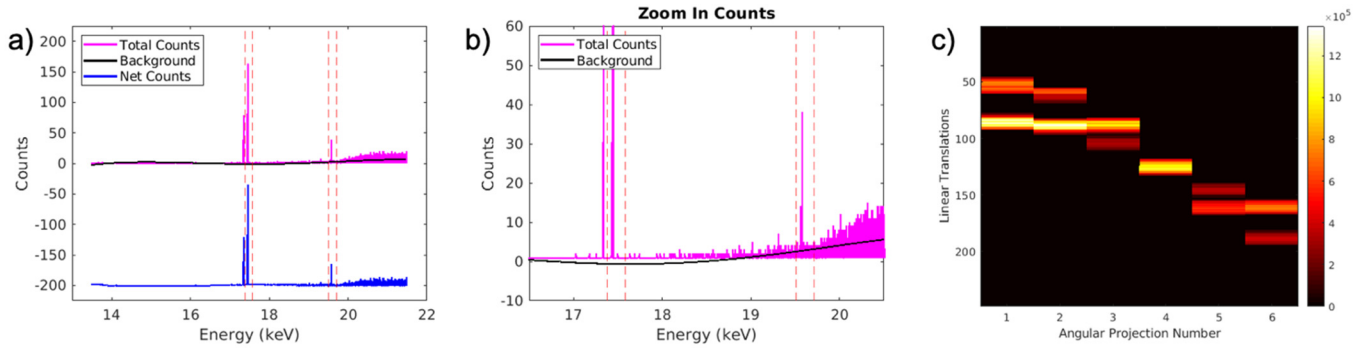

Figure 4. (**a**) A typical example of the removal of the scattered X-ray photons. (**b**) Zoomed-in image to show the removal of the scattered X-ray photons in the K-shell energy range of the MoNP nanoparticles. (**c**) Corrected sinogram summed over all 20 detectors. The detector energy resolution is depicted by the width of the red dashed lines (200 eV).

2.2. System Matrix and Reconstruction Algorithms

To reconstruct the image, an iterative reconstruction approach was taken in which a system of equations $Ax = b$ must be solved, where A is the system matrix, x is the XFCT image, and b is the measurement. To generate the system matrix, the physical process and the imaging geometric parameters were considered. In XFCT imaging, the X-ray beam scans the object along a straight line, and the X-ray beam intensity distribution along the beam line follows the Beer–Lambert law. Upon X-ray beam excitation, target nanoparticles emit isotropic fluorescent X-ray lines. The intensity distribution of fluorescent X-ray lines that span the detector surface similarly follow the Beer–Lambert law. The system matrix is composed of these excitation and sensitivity matrices (F and P, respectively) as follows:

$$\mathrm{F_{j,m}} = \exp\left(\sum -\mu_e(\mathbf{r}) \times \mathrm{L}(\mathbf{r})\right) \tag{1}$$

$$\mathrm{P_{i,m}} = \sum_{1}^{d_n} \exp\left(\sum -\mu_f(\mathbf{r}) \times \mathrm{L}(\mathbf{r})\right) \tag{2}$$

$$\mathbf{A}_{\mathrm{n_d \times I \times J,m}} = \begin{bmatrix} \begin{bmatrix} \mathrm{P_{1,m}} \\ \vdots \\ \mathrm{P_{n_d},}_m \end{bmatrix} \otimes \mathrm{F_{1,m}} \\ \vdots \\ \begin{bmatrix} \mathrm{P_{1,m}} \\ \vdots \\ \mathrm{P_{n_d},}_m \end{bmatrix} \otimes \mathrm{F_{I \times J,m}} \end{bmatrix} \tag{3}$$

$$0 \leq \mathbf{A}_{\mathrm{n_d \times I \times J,m}} \leq 1$$

$\mu_e(\mathbf{r})$ is the linear attenuation coefficients of the imaging object and targets at the excitation energy. $\mu_\mathbf{f}(\mathbf{r})$ is the linear attenuation coefficients of the imaging object and targets at the fluorescent energy. $\mathrm{L}(\mathbf{r})$ is the distance from the start of the X-ray beam or fluorescent emission to the position $\mathbf{r}$. $\mathrm{d_n}$ is the discretization number of the detector surface for which the fluorescent X-ray lines will be accounted for. $\otimes$ represents the element product between $\mathrm{P_{i,m}}$ and $\mathrm{F_{j,m}}$, where $\mathrm{i} \in [1, \mathrm{n_d}]$ is the detector number, $\mathrm{j} \in [1,\ \mathrm{I} \times \mathrm{J}]$ is the excitation scan number, and m is the number of pixels used to discretize the object space. $\mathrm{I} \times \mathrm{J}$ is the product between angular projections number (I) and linear translation steps (J) of each angular projection, respectively. The forward model then becomes:

$$\mathbf{A}_{\mathrm{n_d \times I \times J,m}}\, \mathbf{X}_{\mathrm{m,1}} = \mathbf{B}_{\mathrm{n_d \times I \times J,1}} \tag{4}$$

where $\mathbf{X_{m,1}}$ is the unknown image vector to reconstruct and $\mathbf{B_{n_d \times I \times J,1}}$ is the set of measurements.

The XFCT reconstruction can then be solved by minimizing the following optimization problem with the nonnegativity constraint:

$$\hat{\mathbf{X}} = \underset{\mathbf{x} \geq 0}{\operatorname{argmin}} \mathbf{Q}(\mathbf{x}) := \frac{1}{2}\|\mathbf{B} - \mathbf{A}\mathbf{X}\|_2^2 + \lambda \|\mathbf{X}\|_1^1 \quad (5)$$

where λ is the regularization parameter and $\|\mathbf{X}\|_1^1$ is the L^1 norm of the image vector $\mathbf{X}$. The fNUMOS algorithm is applied to minimize the L^1 regularized difference between the measurements modeled in GATE and the system matrix estimates. The details of the fNUMOS algorithm are explained in detail in [16,17]. The L^1 regularization term is employed since it is well known for sparsity enhancement [15,16]. The system matrix generation and image reconstruction using fNUMOS was performed in MATLAB.

The FBP algorithm employed the Hann filter and used the sinogram data as the input. The ML-EM based XFCT image reconstruction was performed with the system matrix as described in Equation (3), in which the anatomical guidance was included (the F vectors). The general form of the ML-EM algorithm was used, in which no regularization scheme was applied. Both FBP and ML-EM algorithms were performed using the Michigan image reconstruction toolbox (MIRT) in MATLAB [21]. In this work, 15 iterations were performed by the ML-EM algorithm. A greater number of iterations in the ML-EM algorithm gave no significant benefit in the image quality metrics presented in Section 2.6.

2.3. High Spatial Resolution Imaging

To explore the high spatial resolution imaging capabilities of the imaging setup, small target sizes were used in the phantom. In the first case, the targets were set to have a diameter of 0.50 mm with target edge-to-edge distance equal to 0.50 mm. In the second case, the targets were set to have a diameter of 0.25 mm with target edge-to-edge distance equal to 0.25 mm. For high spatial resolution target reconstruction, the image space was discretized into 600 × 600 pixels, with a pixel size of 0.05 mm. To measure the image quality of the reconstruction with the small targets, square regions of interest (ROIs) with sizes of 2 × 2 and 4 × 4 pixel regions were used for 0.25 mm and 0.50 mm diameter targets, respectively.

2.4. Reconstruction Algorithm Performance with Different Angular Projection Number

To explore the robustness of the algorithm to the number of angular projections of measurements, the angular projection number varied from 3 to 10. The detector number also varied from 20 detectors to 2 detectors. The 2-detector configuration was determined based on the configuration that gave the best image quality. The target size was set to be 0.50 mm in diameter.

2.5. Reconstruction Algorithm Comparison

To explore the quality of the fNUMOS image reconstruction, the fNUMOS image reconstruction was compared to the ML-EM and FBP image reconstruction, which were based on the 20-detector configuration and six angular projections. For the FBP algorithm, the Hann filter was implemented in the FBP algorithm.

2.6. Image Quality Evaluation Criteria

Four criteria were used to evaluate the quality of the reconstructed images: target contrast ratio, Dice similarity coefficient, mean squared error (MSE), and contrast noise ratio (CNR).

A target contrast ratio was calculated to determine the proportionality of the contrast signals between the targets by taking the ratio of the contrast of the 10 mg/mL concentration target (T2) to the 5 mg/mL concentration target (T1). For this simulation, the closer the

target contrast ratio is to two, the better. To measure the contrast signal from each target, the mean of a 5 × 5 pixel region of interest was taken from the reconstructed target center.

The Dice similarity coefficient (DICE) was used to measure the accuracy of the reconstructed target localization by comparing the reconstructed and true target positioning [9,17].

$$\mathrm{DICE} = \frac{2 \times |\mathrm{ROI_r} \cap \mathrm{ROI_t}|}{|\mathrm{ROI_r}| + |\mathrm{ROI_t}|} \times 100\% \tag{6}$$

where $\mathrm{ROI_r}$ is the reconstructed target region of interest (ROI), defined as the pixels with intensities greater than 10% of the maximum pixel intensity. For smaller targets, the $\mathrm{ROI_r}$ is defined as the pixels with intensities greater than 20% of the maximum pixel intensity. $\mathrm{ROI_t}$ is the true target region of interest. Generally, the closer DICE is to 100%, the better.

The MSE was used to measure the difference between the normalized reconstruction and normalized ground truth [17].

$$\mathrm{MSE} = \frac{1}{N} \sum_{i=1}^{N} (x_i - x_{0i})^2 \tag{7}$$

where x and x_0 are the normalized reconstructed and true target signal, respectively. N is the number of image pixels. The smaller the MSE, the better.

The CNR measures the level of distinction between the reconstructed targets and the background [17].

$$\mathrm{CNR} = \frac{\bar{x}_{\mathrm{ROI}} - \bar{x}_{\mathrm{ROB}}}{\sqrt{\omega_{\mathrm{ROI}} \sigma^2_{\mathrm{ROI}} + (1 - \omega_{\mathrm{ROI}}) \sigma^2_{\mathrm{ROB}}}} \tag{8}$$

where $\bar{x}_{\mathrm{ROI}}$ and $\bar{x}_{\mathrm{ROB}}$ are the mean signal from the target ROI and the mean signal from the background ROI. The target ROI size was a 5 × 5 pixel region at the center of the true target. The background ROI was the region of pixels outside of the target ROI. $\omega_{\mathrm{ROI}} = |\mathrm{ROI}|/(|\mathrm{ROI}| + |\mathrm{ROB}|)$ and $|\cdot|$ is the number of elements. σ^2_{ROI} and σ^2_{ROB} are the variance of the region of interest of the targets and the variance of the region of the interest of the background, respectively. The larger the CNR, the better. In the results section, $\mathrm{CNR_5}$ and $\mathrm{CNR_{10}}$ correspond to the CNR of the 5 mg/mL and 10 mg/mL target, respectively. According to the Rose criterion, CNR values greater than 4 are considered distinguishable from the background [10].

3. Results

To balance precision, computer memory, and computer storage, the data was processed and displayed to 1/1000 precision.

3.1. Effects of Detector Number and Detector Placement

To explore how the number of detectors and their placement along the ring configuration influence the quality of the reconstructed images, the number of detectors used for reconstruction was varied. The results of reconstructed images for four different detector numbers are seen in Figure 5. Zoomed-in target regions are provided, where the green circles represent the true target size and locations. From the dashed blue lines in the zoomed-in images, line profiles are plotted with the intensity values normalized with respect to the max value along the dashed blue line. All four cases were able to completely separate and localize the target signals within the true target region without noise artifacts outside of the true target region. All four cases were able to reconstruct good target signals, except the case of the two-detector configuration.

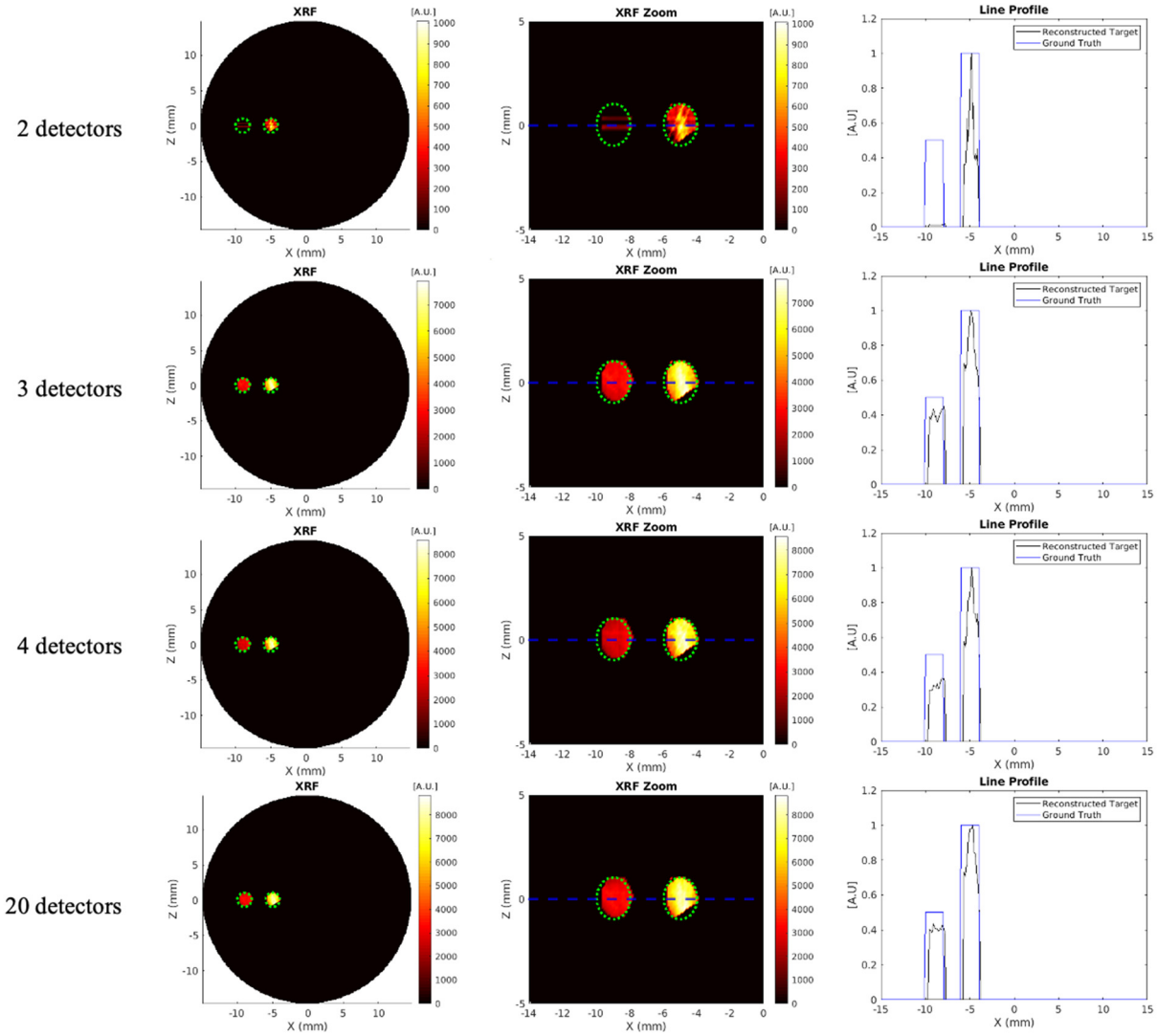

Figure 5. fNUMOS image reconstruction using different detector numbers. The full image (**left**), zoomed-in target regions (**middle**), and line profiles (**right**) are shown. The green dotted line in the zoomed-in target region indicates the exact target size and position; the blue dotted line indicates the line profile location.

The image quality metrics for the reconstruction with 2, 3, 4, and 20 detectors at different positions are listed in Table 1. All detector positions except for the two-detector configuration using the D0 and D4 detectors achieved a DICE coefficient of 88.737%. The two-detector configuration also showed the worst MSE. All targets were evaluated as distinguishable from the background based on the Rose criterion except for the 5 mg/mL target from the two-detector configuration. When the two-detector configuration was changed to the D9 and D14 detectors, the DICE improved from 71.805% to 88.737%. The target contrast ratio also improved from 6.910 to 2.415 when using the D9 and D14 detector configuration. For the three-detector configuration, the detectors D3, D12, and D17 provided a more accurate target contrast ratio than the D0, D9, and D14 detectors. For the four-detector configuration, the D3, D8, D13, and D18 detectors provided a more accurate target contrast ratio than the D0, D5, D10, and D15 detectors. The improvements in the image quality metrics between varying detector positions highlights the importance of detector position in XFCT imaging. The results indicate that two detectors are enough to reconstruct the targets with a DICE of up to 88.737%; however, the accuracy of the reconstruction is strongly dependent on the detector position and the number of angular

projections, as seen in Table 1. It is observed that placing detectors at approximately 180° and 90° from the incident beam trajectory is best for the two-detector case.

Table 1. Image quality metrics for the GATE simulations with varying ring detector element number and position. * = the image quality metrics of the images in Figure 5.

Detector Number	Target Contrast Ratio (Ground Truth = 2)	DICE (%) (Ground Truth = 100%)	MSE	CNR_5, CNR_{10}
2 (D0, D4) *	6.910	71.805	2.229×10^{-3}	1.649, 11.396
2 (D9, D14)	2.415	88.737	1.105×10^{-3}	38.267, 92.413
3 (D0, D9, D14) *	2.430	88.737	1.113×10^{-3}	37.418, 90.907
3 (D3, D12, D17)	2.025	88.737	1.078×10^{-3}	18.196, 36.840
4 (D0, D5, D10, D15) *	2.887	88.737	1.116×10^{-3}	24.616, 71.068
4 (D3, D8, D13, D18)	1.774	88.737	1.030×10^{-3}	24.567, 43.577
20 (D0 to D19) *	2.389	88.737	1.061×10^{-3}	43.516, 103.936

3.2. Reconstruction Algorithm Comparison

Figure 6 shows the reconstructed images and target line profiles of the fNUMOS, ML-EM, and FBP algorithms. In general, the fNUMOS algorithm was superior in terms of achieving a uniform target signal reconstruction with no background noise and target signal that were proportional to their respective concentrations of 5 mg/mL and 10 mg/mL. Neither the ML-EM nor FBP algorithms were able to reconstruct the target signals with intensities proportional to the target concentrations.

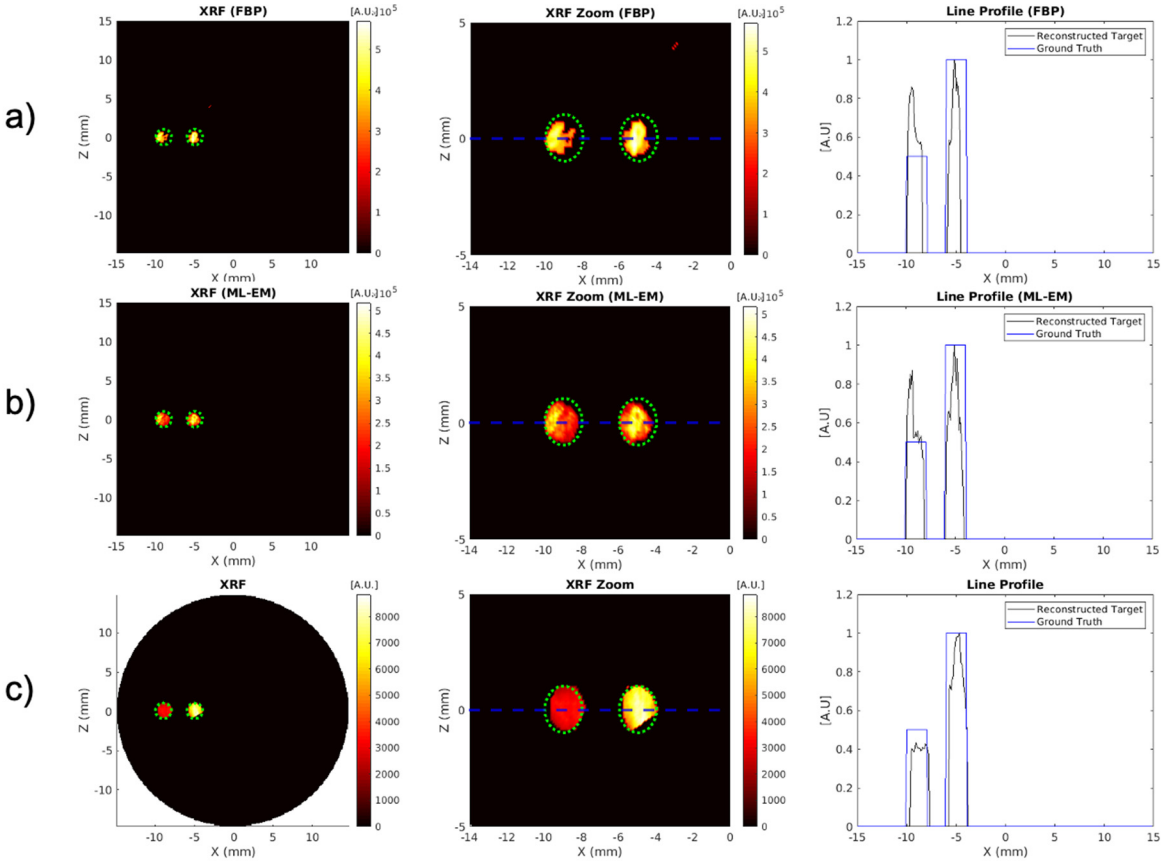

Figure 6. (**a**) Image reconstruction results using FBP. (**b**) Image reconstruction results using ML-EM. (**c**) Image reconstruction results using fNUMOS. All reconstruction algorithms utilized all 20 detectors from the ring detector configuration.

Table 2 shows the image quality metrics of reconstructed images from the fNUMOS, ML-EM, and FBP algorithms. From the Rose criterion, only the 5 mg/mL from the FBP was determined to be indistinguishable from the background. The ML-EM algorithm gave the best DICE. The DICE coefficient from the FBP reconstruction was inferior to ML-EM and fNUMOS. The FBP algorithm also showed the worst MSE from the algorithms. The combination of the accuracy of the target contrast ratio, DICE coefficient, MSE, and CNR values shows that the fNUMOS outperformed the other algorithms. The target contrast ratio, MSE, and CNR values were best with the fNUMOS algorithm.

Table 2. Image quality metrics for the GATE simulations with FBP, ML-EM, and fNUMOS reconstruction.

Reconstruction Method	Reconstruction Time (s)	Target Contrast Ratio (Ground Truth = 2)	DICE (%) (Ground Truth = 100%)	MSE	CNR_5, CNR_{10}
FBP	0.479048	2.410	64.918	2.422×10^{-3}	2.447, 5.897
ML-EM	661.2517	1.5713	89.170	1.645×10^{-3}	12.879, 20.237
fNUMOS	0.015264	2.389	88.737	1.061×10^{-3}	43.516, 103.936

It is also worth noting the time taken for the reconstruction algorithms to reach their solutions. The fNUMOS algorithm took <0.05 s to successfully reconstruct the 300 × 300 pixel XFCT image using the data collected by all 20 detectors in the ring configuration. The ML-EM algorithm took >10 min and the FBP algorithm took <0.5 s to reconstruct the same image, with overall image quality below that of the fNUMOS reconstruction.

3.3. High Spatial Resolution Imaging

Figure 7 shows the reconstructed images, and the target line profiles for the small targets. Due to the size of the targets, slight background noise is noticeable in the reconstructed images; however, clear target separation is still achieved, as seen in the images and the line profiles.

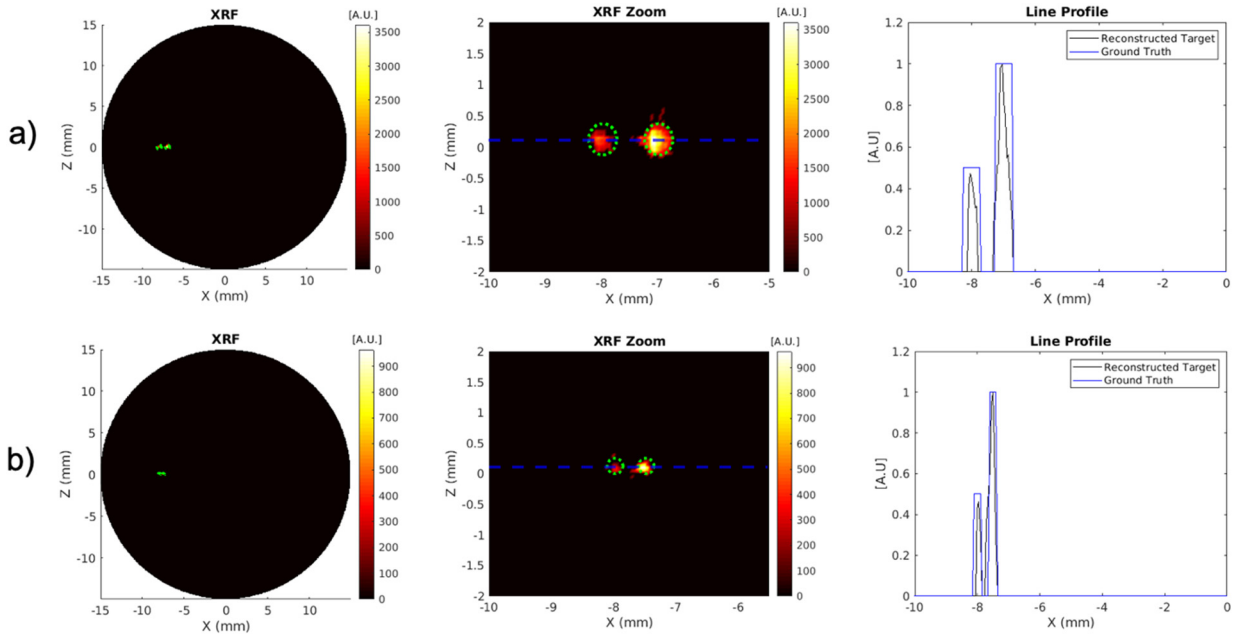

Figure 7. fNUMOS reconstruction of small targets. (**a**) Image reconstruction of the 0.50 mm diameter targets. (**b**) Image reconstruction of the 0.25 mm diameter targets. The reconstructions used all 20 detectors from the detector ring configuration.

Table 3 shows the image quality metrics for high spatial resolution imaging of the small targets. The detector number also varied from 20 detectors to two detectors. The two-

detector configuration used detectors of D9 and D14, which was the detector configuration with the best image quality metrics from Table 1.

Table 3. High spatial resolution imaging metrics with varying target size and detector number.

Target Size (mm)	Detector Number	Target Contrast Ratio (Ground Truth = 2)	DICE (%) (Ground Truth = 100%)	MSE	CNR_5, CNR_{10}
0.25	20 (D0 to D19)	2.981	38.89	5.710×10^{-5}	4.650, 13.861
	2 (D9, D14)	4.071	37.68	5.796×10^{-5}	2.003, 8.153
0.50	20 (D0 to D19)	2.030	66.67	1.197×10^{-4}	7.445, 15.110
	2 (D9, D14)	1.662	67.13	1.283×10^{-4}	5.474, 9.098

For the 0.25 mm target reconstruction, the target contrast ratios are 2.981 and 4.071 for the 20-detector and two-detector configuration, respectively. The DICE coefficients are 38.89% and 37.68% for the 20-detector and two-detector configuration, respectively. The MSE of the 20-detector configuration and the two-detector configuration are similar. For the 20-detector configuration, both targets are distinguishable from the background according to the Rose criterion. For the two-detector configuration, the 5 mg/mL target is indistinguishable from the background.

For the 0.50 mm target reconstruction, the target contrast ratios are 2.030 and 1.662 for the 20-detector and two-detector configuration, respectively. The DICE coefficient of the 0.50 mm target is slightly better with the two-detector configuration than the 20-detector configuration. MSE and CNR values are the best for the 0.50 mm targets with the 20-detector configuration. When considering the combination of the image quality metrics, the most accurate reconstruction for high spatial resolution is obtained when using the 20-detector configuration and 0.50 mm diameter targets. The least accurate reconstruction for high spatial resolution is obtained with the 0.25 mm targets when using the D9 and D14 detector configuration.

3.4. Reconstruction Algorithm Performance with Different Angular Projection Number

Table 4 shows the image quality metrics with varying angular projection numbers and detector numbers. The two-detector configuration used detectors of D9 and D14, which is the detector configuration with the best image quality metrics from Table 1. The most accurate reconstruction was achieved with 10 angular projections with detectors D9 and D14 when considering the target contrast ratio, DICE, MSE, and CNR values. The MSE and CNR values are best with 10 angular projections and the two-detector configuration. The least accurate reconstruction was achieved with three angular projections and detectors D9 and D14, which showed the worst MSE and target contrast ratio, lowest DICE, and lowest CNR values. The 5 mg/mL target reconstruction with three angular projections and the two-detector configuration was determined to be indistinguishable from the background. The best DICE was achieved with six angular projections with the 20-detector configuration. From Table 4, we see that the reconstructed XFCT image quality is good with 20 detectors and is not very good with two detectors when the angular projection number is three, which is reasonable. The reconstructed XFCT images are good when the angular projection number is six or 10 for both two detectors and 20 detectors. Note that while the Rose criterion is preserved, the improvement of DICE and target contrast ratio is not significant for the 20-detector case compared to the two-detector case if the angular projection number is six or 10. This means that a large number of detectors is not needed if six angular projections are performed.

Table 4. Image quality metrics with varying angular projection number and detector number.

Number of Projections	Detector Number	Target Contrast Ratio (Ground Truth = 2)	DICE (%) (Ground Truth = 100%)	MSE	CNR_5, CNR_{10}
3	20 (D0 to D19)	2.201	55.07	1.874×10^{-4}	15.208, 33.476
	2 (D9, D14)	3.220	49.18	1.993×10^{-4}	2.066, 6.654
6	20 (D0 to D19)	1.825	65.67	1.528×10^{-4}	4.923, 8.983
	2 (D9, D14)	1.750	53.97	1.763×10^{-4}	4.859, 8.506
10	20 (D0 to D19)	2.186	57.14	1.472×10^{-4}	32.853, 71.801
	2 (D9, D14)	2.161	59.62	1.377×10^{-4}	61.394, 132.651

4. Discussion

In this work, a benchtop XFCT imaging system comprised of ring detector elements and a benchtop quasi-monochromatic source was modeled in GATE. The fNUMOS algorithm was applied to reconstruct the image successfully and efficiently. The fNUMOS algorithm was successful in localizing small targets as well. Due to the unique energy characteristics of the benchtop source, a relatively low X-ray photon number was enough to obtain a good XFCT signal even when a low number of detectors from the ring configuration were used. If a conventional polychromatic source were to be used instead, the number of X-rays would need to be increased to obtain sufficient fluorescent counts for a good image reconstruction since the bremsstrahlung energies would mainly contribute to dose.

The proposed imaging scheme and reconstruction algorithm was studied with different detector numbers and detector positions, and different angular projection numbers. Compton scattering effects prevent a good and clear XFCT signal from being detected. Detector placement is crucial to minimizing the detection of greater scattering counts. Typically, detectors are placed >90° to the incident beam trajectory to minimize scatter. In this work, it was shown that two detectors are enough to accurately reconstruct the targets; however, the accuracy of the reconstruction is strongly dependent on the placement of the detectors and the number of angular projections, as seen in Tables 1 and 4. Placing detectors at approximately 180° and 90° from the incident beam trajectory is best for the two-detector case. This recommendation is supported by other literature [4,5,12]. When considering the imaging protocol and dose concerns with pencil-beam XFCT imaging, six angular projections are sufficient to provide an accurate reconstruction of small targets. However, when utilizing the full ring configuration with 20 detectors, three angular projections are enough for an accurate reconstruction based on the image quality metrics.

Several artifacts can be observed in Figure 5. In the two-detector configuration, the artifacts resulted from bad detector placement, in which the reconstructed targets had a nonuniform signal intensity. From detector configurations 3, 4, and 20, the artifacts are the slight signal nonuniformity in the right target and the missed target signals in the bottom right of the right target. These artifacts were likely caused by the combination of the limited projection number and the scatter noises. It is well known that measurements at each projection takes a very long time to measure. It is a compromise between the measurement time (projection number) and the image quality [6].

From the image quality metrics in Table 3, the target contrast ratio retained proportionality of the reconstructed signals, whereas the CNR and DICE image quality metrics suffered. These results are due to the increased sparsity of the problem. With the 2 mm targets, the incident beam linearly projected at most 16 times on each target. For the 0.50 and 0.25 mm targets, the incident beam linearly projected at most four and two times on each target, respectively. The reduction of the beam incident on the targets resulted in significantly less fluorescent X-rays for an accurate reconstruction. Nonetheless, the fNUMOS algorithm was able to localize the signal from the small targets within the true target region.

The fNUMOS reconstruction algorithm performance was compared with the popular ML-EM and FBP algorithms. The image quality metrics show that the fNUMOS reconstruc-

tion algorithm is superior when considering the combination of the target contrast ratio, DICE coefficient measurements, CNR values, MSE, and reconstruction time. The XFCT measurements only have six angular projections, which is why artifacts in the reconstructed XFCT images by FBP are observed. Unlike the FBP and ML-EM, the fNUMOS algorithm performs well with sparse targets with little computation time, as seen in this work and in XLCT studies [14,15], because there is L^1 regularization in the fNUMOS algorithm.

5. Conclusions

In summary, a benchtop pencil-beam XFCT imaging system with a ring detector and a unique quasi-monochromatic benchtop source was proposed. GATE simulations were performed to validate the forward modeling and the fNUNMOS-based XFCT reconstruction algorithm. Our simulation results indicate that a quasi-monochromatic source from Sigray and a 20-detector ring could be used to improve the performance of the proposed XFCT imaging system. In the future, we plan to collaborate with the Sigray company to design and build a benchtop XFCT system with good spatial resolution and practical scanning times for small animal XFCT imaging.

Author Contributions: Data curation, Y.F. and M.L.; Formal analysis, I.O.R. and M.L.; Methodology, I.O.R.; Supervision, C.L.; Writing—original draft, I.O.R.; Writing—review & editing, C.L. All authors have read and agreed to the published version of the manuscript.

Funding: This work was funded by the NIH National Institute of Biomedical Imaging and Bioengineering (NIBIB) [R01EB026646].

Institutional Review Board Statement: Not applicable.

Informed Consent Statement: Not applicable.

Data Availability Statement: The GATE Monte Carlo code can be found in https://github.com/OpenGATE/Gate (accessed 22 June 2021). The XFCT data can be accessible upon request.

Acknowledgments: The authors thank Sigray, Inc. for providing the spectral information of the Sigray X-ray source.

Conflicts of Interest: The authors declare no conflict of interest.

References

1. Deng, L.; Ahmed, M.F.; Jayarathna, S.; Feng, P.; Wei, B.; Cho, S.H. A detector's eye view (DEV)-based OSEM algorithm for benchtop X-ray fluorescence computed tomography (XFCT) image reconstruction. *Phys. Med. Biol.* **2019**, *64*. [CrossRef] [PubMed]
2. Zhang, S.; Li, L.; Chen, J.; Chen, Z.; Zhang, W.; Lu, H. Quantitative imaging of gd nanoparticles in mice using benchtop cone-beam X-ray fluorescence computed tomography system. *Int. J. Mol. Sci.* **2019**, *20*, 2315. [CrossRef] [PubMed]
3. Jones, B.L.; Cho, S.H. The feasibility of polychromatic cone-beam X-ray fluorescence computed tomography (XFCT) imaging of gold nanoparticle-loaded objects: A Monte Carlo study. *Phys. Med. Biol.* **2011**, *56*, 37193730. [CrossRef] [PubMed]
4. Dunning, C.A.S.; Bazalova-Carter, M. Optimization of a table-top X-ray fluorescence computed tomography (XFCT) system. *Phys. Med. Biol.* **2018**, *63*, 235013. [CrossRef] [PubMed]
5. Vernekohl, D.; Xing, L. X-ray Excited Fluorescent Materials for Medical Application. *Top. Med. Chem.* **2014**, *9*, 1–68. [CrossRef]
6. Larsson, J.C.; Vogt, C.; Vågberg, W.; Toprak, M.S.; Dzieran, J.; Arsenian-Henriksson, M.; Hertz, H.M. High-spatial-resolution X-ray fluorescence tomography with spectrally matched nanoparticles. *Phys. Med. Biol.* **2018**, *63*. [CrossRef] [PubMed]
7. Shilo, M.; Reuveni, T.; Motiei, M.; Popovtzer, R. Nanoparticles as computed tomography contrast agents: Current status and future perspectives. *Nanomedicine* **2012**, *7*. [CrossRef] [PubMed]
8. Hainfeld, J.F.; Slatkin, D.N.; Smilowitz, H.M. The use of gold nanoparticles to enhance radiotherapy in mice. *Phys. Med. Biol.* **2004**, *49*. [CrossRef] [PubMed]
9. Jiang, S.; He, P.; Deng, L.; Chen, M.; Wei, B. Monte Carlo Simulation for Polychromatic X-ray Fluorescence Computed Tomography with Sheet-Beam Geometry. *Int. J. Biomed. Imaging* **2017**, *2017*. [CrossRef] [PubMed]
10. Bazalova, M.; Kuang, Y.; Pratx, G.; Xing, L. Investigation of X-ray fluorescence computed tomography (XFCT) and K-edge imaging. *IEEE Trans. Med. Imaging* **2012**, *31*, 1620–1627. [CrossRef] [PubMed]
11. Cheong, S.K.; Jones, B.L.; KSiddiqi, A.; Liu, F.; Manohar, N.; Cho, S.H. X-ray fluorescence computed tomography (XFCT) imaging of gold nanoparticle-loaded objects using 110 kVp X-rays. *Phys. Med. Biol.* **2010**, *55*, 647–662. [CrossRef] [PubMed]
12. Dunning, C.A.S.; Bazalova, M. Design of a combined X-ray fluorescence Computed Tomography (CT) and photon-counting CT table-top imaging system. *J. Instrum.* **2020**, *15*, P06031. [CrossRef]

13. Defrise, M.; Kinahan, P.E.; Michel, C.J. Image Reconstruction Algorithms in PET. In *Positron Emission Tomography*; Bailey, D.L., Townsend, D.W., Valk, P.E., Maisey, M.N., Eds.; Springer: London, UK, 2005.
14. Zhang, W.; Romero, I.O.; Li, C. Time domain X-ray luminescence computed tomography: Numerical simulations. *Biomed. Opt. Express.* **2019**, *10*, 372. [CrossRef] [PubMed]
15. Li, C.; Martínez-Dávalos, A.; Cherry, S.R. Numerical simulation of X-ray luminescence optical tomography for small-animal imaging. *J. Biomed. Opt.* **2014**, *19*, 046002. [CrossRef] [PubMed]
16. Zhu, D.; Li, C. Nonconvex regularizations in fluorescence molecular tomography for sparsity enhancement. *Phys. Med. Biol.* **2014**, *59*, 2901–2912. [CrossRef] [PubMed]
17. Zhu, D.; Li, C. Accelerated image reconstruction in fluorescence molecular tomography using a nonuniform updating scheme with momentum and ordered subsets methods. *J. Biomed. Opt.* **2016**, *21*, 016004. [CrossRef] [PubMed]
18. Jan, S.; Santin, G.; Strul, D.; Staelens, S.; Assié, K.; Autret, D.; Avner, S.; Barbier, R.; Bardiès, M.; Bloomfield, P.M.; et al. GATE: A simulation toolkit for PET and SPECT. *Phys. Med. Biol.* **2004**, *49*, 4543–4561. [CrossRef] [PubMed]
19. Achterhold, K.; Bech, M.; Schleede, S.; Potdevin, G.; Ruth, R.; Loewen, R.; Pfeiffer, F. Monochromatic computed tomography with a compact laser-driven X-ray source. *Sci. Rep.* **2013**, *3*, 3–6. [CrossRef] [PubMed]
20. Brun, R.; Rademakers, F. ROOT-An Object Oriented Data Analysis Framework, Proceedings AIHENP'96 Workshop, Lausanne, September 1996. *Nucl. Inst. Methods Phys. Res. A* **1997**, *389*, 81–86. Available online: http://root.cern.ch/ (accessed on 18 June 2021). [CrossRef]
21. Fessler, J.A. Michigan Image Reconstruction Toolbox. Available online: https://web.eecs.umich.edu/~fessler/code/index.html (accessed on 18 June 2021).